

Shot noise in Aharonov-Bohm interferometers: Comparison of helical and conventional setups

R. A. Niyazov,^{1,2} I. V. Krainov,² D. N. Aristov,^{1,2,3} and V. Yu. Kachorovskii²

¹*NRC “Kurchatov Institute”, Petersburg Nuclear Physics Institute, Gatchina 188300, Russia*

²*Ioffe Institute, 194021 St. Petersburg, Russia*

³*Department of Physics, St. Petersburg State University, St. Petersburg 199034, Russia*

We study the shot noise of current through the edge states of a two-dimensional topological insulator placed in magnetic field and compare the obtained results with the shot noise in conventional single-channel spinless Aharonov-Bohm interferometer. We find general formulas for the Fano factors of these setups, assuming that temperature exceeds level spacing in the system. We demonstrate that both in helical and in conventional case the interference effects dramatically change the Fano factor and its magnetic field dependence. For weak tunneling coupling with leads, the Fano factors of both setups exhibit a periodic series of sharp Aharonov-Bohm peaks with variation of magnetic flux piercing the system. Our key finding is that the Fano factor in the helical interferometer provides information about the presence of backscattering defects violating topological protection. In particular, the amplitude of Aharonov-Bohm peaks in the helical setup is proportional to the strength of the defect in contrast to conventional setup, where peaks have finite amplitude even in the ballistic case.

I. INTRODUCTION

Quantum interferometry is a rapidly growing area of electronics with a huge potential for practical use, in particular, in the booming fields of quantum computing and quantum cryptography. One beautiful manifestation of quantum interference is the Aharonov-Bohm effect [1, 2]—the sensitivity of the phase of electron wave function to magnetic flux. Quantum interferometers based on this effect are used for high-precision measurements of magnetic fields, for example, by using SQUID circuits.

The simplest setup to study interference and particularly the Aharonov-Bohm effect is a ring-shaped interferometer with two single-channel arms placed in the perpendicular magnetic field. Due to the interference of electron trajectories winding around such a setup, the observables, like transmission coefficient and the noise intensity, show Aharonov-Bohm oscillations with a certain period $\Delta\phi$ as a function of dimensionless magnetic flux $\phi = \Phi/\Phi_0$ threading the device, where $\Phi_0 = hc/e$ is the flux quantum. The key statement of our paper is that noise in such a simple system is still not well understood and depends on specific realizations of the single-channel arms.

Below we will investigate and compare in details two types of setups: (i) a spinless single-channel interferometer based on conventional materials (CI), i.e. a single-channel spinless quantum wire, folded in a ring-like shape and having two tunnel or metallic contacts attached (see Fig. 1a); (ii) an interferometer based on helical edge states (HI). The latter interferometer can be implemented in two-dimensional topological insulators [3], which are insulators in the bulk, but have helical one-dimensional (1D) edge states conducting the current without dissipation [3–5]. These edge states are formed by electrons with opposite spins travelling in opposite directions, so that backscattering by non-magnetic impurities is prohibited. If one attaches two contacts to the

edge and apply the gate voltage to shift the Fermi level into the band gap, then the conductance of such a device is fully determined by the edge states (see Fig. 1b). Since the sample boundary can be bypassed in two directions, possibly with several windings, such a system represents an interferometer that encodes information about properties of the helical edge states (HES).

Both setups, CI and HI, have two electron waves propagating clockwise and counterclockwise in 1D channel. However, the interference phenomena in these systems manifest themselves in a rather different way. Most interestingly, in case of ballistic HI, the waves propagating in opposite directions have also opposite spin projections and cannot interfere provided that contacts to the HES are non-magnetic. Interference effects in HI appear in the presence of backscattering. This means that the observation of interference phenomena in the HI can give information about mechanisms of possible violation of the topological protection. By contrast, a spinless CI based on conventional materials (Fig. 1a) shows interference effects even in the ballistic case, because non-magnetic contacts in such setup lead to backscattering. Hence, ballistic CI is analogous to HI with a magnetic defect (or with one or two magnetic contacts), see Fig. 1b. We will also demonstrate that $\Delta\phi$ is different in these cases: $\Delta\phi = 1$ for CI and $\Delta\phi = 1/2$ for HI with a single static magnetic defect.

For both setups we will investigate the manifestations of quantum interference in the shot noise of the current. Such noise is a consequence of the discreteness of the electron charge. Importantly, its measurement provides information not available from conductance measurements: namely, the charge and statistics of current carriers, and the internal energy scales of the system [6, 7]. Our primary goal is to calculate the Fano factor, \mathcal{F} , which is the ratio of the shot noise and the so-called Schottky noise value. This ratio is often used to characterize different transport regimes. For example, the values $\mathcal{F} = 1/3$

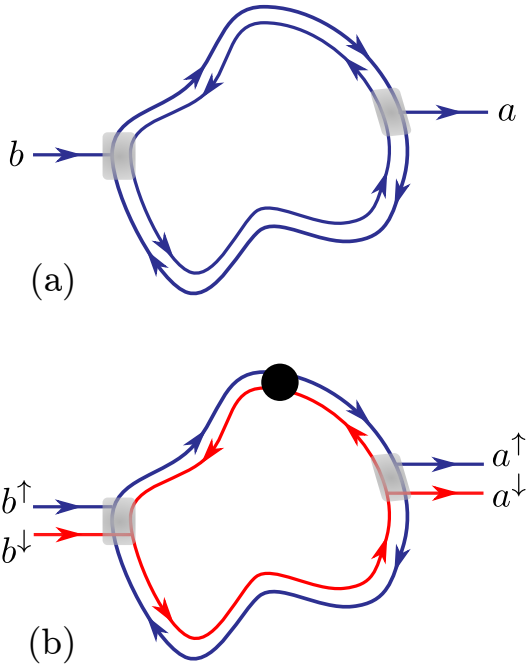


FIG. 1. Aharonov-Bohm interferometers based on conventional spinless single-channel quantum wire (a) and on helical edge channels of 2D topological insulator (b). The leads (shown by grey color) are modeled by conventional single-channel [spinless (a) and spinfull (b)] wires. The black dot in panel (b) represents a magnetic impurity. Grey regions represent contacts described by 3×3 and 4×4 S -matrix for CI and HI, respectively [see Eqs. (2), (3) and Figs. 2, 4].

and $\mathcal{F} = 1/2$ for a diffusive conductor and tunneling transmission through a quantum level, respectively, are universal and independent of the system details [6, 7].

Since the conductance and shot noise of interferometers of various types were studied in a great number of works, we will start with a short description of the state of the art. Let us first recall the key results known for the conductance of the Aharonov-Bohm interferometer. At weak tunnel coupling and at low temperatures, the conductance $G(\phi)$ exhibits sharp resonances at certain values of magnetic flux, arising when quantum levels of the system are crossed by the Fermi level [8, 9]. The case of relatively high temperatures, T , is much less trivial. One might expect that interference is suppressed when T becomes larger than the level spacing, Δ . As was shown theoretically this is not the case neither for CI [10–15] nor for HI [16–19], and the interference effects “survive” even in the case

$$T \gg \Delta = 2\pi v_F/L, \quad (1)$$

where $L = L_1 + L_2$, with $L_{1,2}$ the lengths of the interferometer arms, and v_F is the Fermi velocity. However, instead of resonances, $G(\phi)$ exhibits narrow antiresonances under the condition (1). Physically, antiresonances arise due to trajectories that interfere destructively at any energy ε and, accordingly, are insensitive to energy averaging

(see discussions in [11] and [16] regarding CI and HI, respectively). For typical v_F of order of 10^7 cm/s and typical system sizes (> 1 micron), the value of Δ does not exceed several degrees Kelvin. This means that the interference effects can be studied at relatively high temperatures, which are relevant for various applications.

The conductance in CI in the temperature range (1) has been studied in detail, in particular, considering the effects of the electron-electron interaction [11], disorder [13], and spin-orbit interaction [12]. Recently, some of these results were generalized to HI systems: to single ring-shaped HI [16–19] with a static magnetic defect and, partially, to arrays of coupled helical rings [20].

The influence of the interference effects on the noise has previously been discussed only in the low-temperature regime, $T \ll \Delta$, see review in Ref. [21] for CI and Refs. [22, 23] for HI. To the best of our knowledge, the effects of the interference for the noise in the high-temperature regime (1) were not discussed in detail for either CI or HI setups. On the other hand there is a clear need of the corresponding theory, which would allow direct comparison with experiment, since nanoscale rings made from conventional materials with a few or single conducting channels have been already fabricated [21–25]. Also, the experiment aimed to study helical interferometers was recently reported [24], although it focused on the low-temperature case. Note that in the latter experiment a quantum point contacts to the HES have been realized, thus allowing experimental verification of interference effects in conductance and noise of tunneling HI, especially having in mind that the condition (1) does not require very strict restrictions on temperature.

It is worth noting that the shot noise in HES has already been discussed for the case of infinite edge [25–35], i.e. without taking into account the interference effects. In particular, a great attention was paid to infinite HES with a dynamic magnetic impurity [29, 31–35]), whose magnetic moment changes direction after each scattering event. Discussing HI in this paper, we focus on the opposite case of static magnetic defect (see discussion of our model in the next section). The experimental measurement of the Fano factor of HI at zero magnetic field for the edge states of 2D TI gives the value $0.1 < \mathcal{F} < 0.3$ [27, 30]. The upper value, 0.3, is close to the value $1/3$ for diffusive conductor. A similar result was obtained in the model with a large number of “islands”, allowing spin relaxation and tunnel-connected to the HES [36]. The effect of islands of different types on HES is currently being actively debated (see [37] and references therein). However, the latter model, among others, does not consider interference effects.

In this paper, we will discuss ballistic CI without impurities and defects and also HI with a single static magnetic defect (MD) placed into one of the arm of the interferometer. The goal of the work is to find the dependence of Fano factor, \mathcal{F} , on tunneling coupling, on the magnetic flux, and, in the case of HI, on the strength of magnetic defect. The latter is characterized by the parameter θ ,

with $\theta = 0$ in the absence of defect, and $\theta = \pi/2$ for the strong, fully reflective defect. We will find general analytical expressions for \mathcal{F}^{CI} , \mathcal{F}^{HI} and analyze simple limiting cases assuming that inequality (1) is satisfied.

II. MODEL

We calculate the current shot noise in the Aharonov-Bohm interferometers of two types: conventional AB interferometer (CI) and helical AB interferometer (HI), depicted in Fig. 1a and Fig. 1b, respectively. They are based on spinless single-channel quantum wire (CI) and helical edge states (HI). We model leads by conventional single-channel wires (spinless or spinfull for the conventional and helical case, respectively). Although this model of the leads is very simplified, it is commonly used in quantum interferometry, starting from the work [8], since, as we demonstrate below, it allows to describe the transition from the metallic leads to the tunnel ones. In particular, this model qualitatively describes quantum point contacts to the interferometer.

A. Conventional AB interferometer

The unitarity of scattering matrix of the contact results in backscattering on the contacts in case of CI [11]. Here, we use this scattering matrix with real-valued elements:

$$\hat{S}^{\text{CI}} = \begin{pmatrix} t_r & t_{\text{out}} & t_{\text{out}} \\ t_{\text{in}} & t_b & t \\ t_{\text{in}} & t & t_b \end{pmatrix}, \quad (2)$$

$$t = \frac{1}{1 + \gamma}, \quad t_b = -\frac{\gamma}{1 + \gamma},$$

$$t_{\text{in}} = t_{\text{out}} = \frac{\sqrt{2\gamma}}{1 + \gamma}, \quad t_r = -\frac{1 - \gamma}{1 + \gamma}.$$

More general case of \hat{S}^{CI} is discussed in Refs. [38] and [39]. The scattering amplitudes entering Eq. (2) obey $2t_{\text{in}}^2 + t_r^2 = t^2 + t_b^2 + t_{\text{out}}^2 = 1$. The meaning of these amplitudes is illustrated in Fig. 2: t_{in} is the amplitude to enter in the interferometer into one of the counter-propagating channels, t_{out} is the amplitude to exit the interferometer, t and t_b are respectively the amplitudes of forward and backward scattering on the contact inside the interferometer, and t_r is the amplitude of backward scattering for electrons coming from the lead. All scattering amplitudes are parameterized by a single parameter $\gamma \in (0, \infty)$.

The meaning of the parameter γ is further illustrated in Fig. 3, see also discussion in Refs. [11, 39, 40]. The case $\gamma \ll 1$ corresponds to tunneling contact, where almost closed interferometer is weakly coupled to the leads, with γ being a tunneling transparency (see Fig. 3a). Interestingly, the case $\gamma \rightarrow \infty$ also corresponds to weak tunneling coupling. However, this case is strongly different from the case $\gamma \rightarrow 0$, as illustrated in Fig. 3b. Metal-

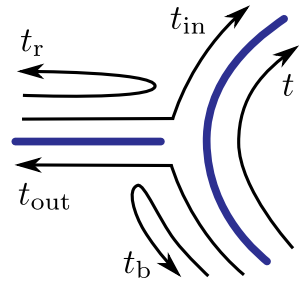


FIG. 2. Scattering amplitudes entering scattering matrix Eq. (2) for CI. The lead is modeled by spinless 1D wire. For tunneling contact, $|t_r| \approx 1$, while the case of metallic contact corresponds to $t_r = 0$.

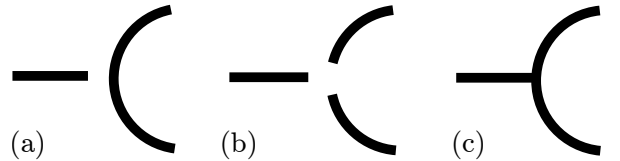


FIG. 3. Schematic illustration of different types of leads: panels (a) and (b) shows two different types of tunneling coupling, corresponding to $\gamma = 0$ and $\gamma = \infty$, respectively; panel (c) illustrates “metallic” contact, $\gamma \approx 1$.

lic contact is modeled by $\gamma \approx 1$ (see Fig. 3c). It is worth noting that $t_b \neq 0$ for any non-zero γ . Below we show that two configurations, Fig. 3a and Fig. 3b, may correspond to the same conductance but to different noise.

B. Helical AB interferometer

Next we discuss model of HI. We consider 2D TI, assuming that the Fermi level is located in the bulk gap, so that the transport between two contacts connected to the system is completely determined by the HES. The simplest scattering matrix of a non-magnetic lead has the

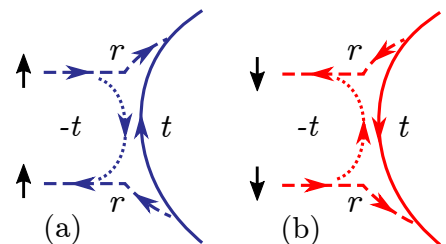


FIG. 4. The scattering amplitudes entering scattering matrix of contacts, Eq. (3), which are modelled as a single-channel spinfull wire. It is assumed that there is no spin flip at the contact and the two spin polarizations at the contact (shown by red and blue color) are completely separated. The $t \rightarrow 1$ case corresponds to a tunnel contact, and the $t \rightarrow 0$ case models a metal contact.

form

$$\hat{S}^{\text{HI}} = \begin{pmatrix} -t & r & 0 & 0 \\ r & t & 0 & 0 \\ 0 & 0 & -t & r \\ 0 & 0 & r & t \end{pmatrix}, \quad t^2 + r^2 = 1, \quad (3)$$

where two identical blocks are responsible for two spins, and the basis is chosen in accordance with the spin polarization of the helical states at the point of contact (red and blue in Fig. 4). It is convenient to parameterize amplitudes t and r by a parameter λ :

$$t = e^{-\lambda}, \quad r = \sqrt{1 - e^{-2\lambda}}, \quad 0 < \lambda < \infty. \quad (4)$$

Importantly, due to the topological protection, backscattering appears in the HI only in presence of magnetic defects or magnetization of the leads. We assume in this paper that the leads are non-magnetic but there is a static magnetic defect in one of the arms of the interferometer. A comment is in order here. As we already mentioned, much attention was drawn recently to the infinite HES with a dynamic magnetic impurity [29, 31–35]), whose magnetic moment changes direction after each scattering event. For the isotropic exchange interaction between the impurity and the HES, the impurity's magnetic moment relaxes within the so-called Korringa time towards the local direction of the electron spin in the HES and, as a consequence, the interaction between the impurity and the HES becomes completely ineffective (see discussion in [29]). Accordingly, the problem of the noise intensity at zero frequency in the HES with a single impurity makes sense only in the presence of an anisotropic exchange interaction [31] (or an external magnetic field acting on a dynamic impurity [35]), while in the limit of isotropic exchange interaction Fano factor is singular [31], i.e. the result for the \mathcal{F} depends on the order in which the constants responsible for the anisotropy tend to zero (see also discussion in [28])

At the same time, the relaxation of the impurity's magnetic moment in reality stems not only from the interaction with the HES, but also from the environment of the impurity, which should provide a non-singular response for the \mathcal{F} even for the isotropic exchange interaction. Therefore, it seems no less interesting to study the case which is opposite to one considered in the papers [29, 31–35], namely, the case of a static magnetic defect with a large spin, which is robustly connected to the external environment.

Such a defect, considered below, ensures the existence of a magnetic field in a small region of the HES, i.e. allows elastic backward scattering without tunneling coupling between the HES and defect.

Specifically, we assume the presence of magnetic defect (MD) at the edge of the TI, which can be, for example, a potential dielectric ferromagnetic point contact with high magnetic stiffness and with the magnetic moment, whose direction is determined by uniaxial anisotropy and the demagnetization tensor of the ferromagnet. We describe

the electron scattering on such MD by the scattering matrix

$$\hat{S}_{\text{MD}} = \begin{pmatrix} \cos \theta e^{i\alpha} & i \sin \theta e^{i\varphi} \\ i \sin \theta e^{-i\varphi} & \cos \theta e^{-i\alpha} \end{pmatrix}, \quad (5)$$

that allows for backward scattering, and neglect the back influence of the HES on the parameters of S_M . The backward scattering rate, $R_\theta = \sin^2 \theta$, is determined by the quantity θ while the phase φ has the meaning of the backward scattering phase on the MD.

Here we derive analytical expressions describing anticrossing of quantum levels of right- and left-moving electrons on the example of a single impurity placed in the upper shoulder. We consider interferometer with the lengths of the upper and lower shoulders given by L_1 and L_2 , respectively. The magnetic impurity is placed at position x_0 such that $0 < x_0 < L_1$. Using expression for scattering matrix (5), one can easily find transfer matrix of impurity

$$\hat{T}_{\text{MD}} = \frac{e^{-i\alpha}}{\cos \theta} \begin{pmatrix} 1 & i \sin \theta e^{-i\xi} \\ -i \sin \theta e^{i\xi} & 1 \end{pmatrix}, \quad (6)$$

where $\xi = \varphi - 2kx_0$ and $k = \varepsilon/v_F$ is the electron wave vector. One can show that the forward scattering phase α can be fully incorporated into the shift of ϕ , so that we put $\alpha = 0$ below.

Note that the possibility of creating static magnetic contacts to the HES has also been discussed in another context [41]. In principle, the interference effects we are interested in could also be observed for a point-like non-magnetic scatterer, taking into account the electron-electron interaction [42]. In the latter case, however, an analysis of inelastic effects is required, which is beyond the scope of the current work.

III. SHOT NOISE AND CONDUCTANCE

A. General equations

In this Section, we calculate \mathcal{F} for setups shown in Fig. 1 assuming that a fixed bias voltage V is applied to leads. We will consider the most interesting and easily realized case:

$$\Delta \ll T \ll eV. \quad (7)$$

The current noise is related with fluctuations of the electric current with respect to its average value $\delta \hat{I}(t) = \hat{I}(t) - \langle \hat{I} \rangle$. Here \hat{I} is the current operator (an analytical expression for \hat{I} is given in [6, 7]). The current correlation function associated with the noise is defined by:

$$\mathcal{S}(t - t') = \frac{1}{2} \langle \delta \hat{I}(t) \delta \hat{I}(t') + \delta \hat{I}(t') \delta \hat{I}(t) \rangle.$$

The Fourier transform of \mathcal{S} gives an expression for the noise power: $S(\omega) = 2 \int_{-\infty}^{\infty} dt e^{i\omega t} \mathcal{S}(t)$ [the factor 2 in

this expression is a matter of convention, see Eq. (1) in Ref. [6] and the comment after Eq. (49) in Ref. [7].

Spin-dependent transport through the two-terminal device is fully characterized by the matrix of transmission amplitudes $\hat{t} = t_{\alpha\beta}$ (here α and β are the spin indices associated with the outgoing and the incoming electrons, respectively) [6, 7]:

$$\mathcal{S}(\omega = 0) = G_0 \int_{\mu}^{\mu+eV} d\varepsilon \text{Tr} \left[\hat{\mathcal{T}}(\varepsilon) \left(1 - \hat{\mathcal{T}}(\varepsilon) \right) \right], \quad (8)$$

where $G_0 = 2e^2/h$ conductance quantum and

$$\hat{\mathcal{T}}(\varepsilon) = \hat{t}(\varepsilon) \hat{t}^\dagger(\varepsilon). \quad (9)$$

The averaged current, $I = \langle \hat{I} \rangle$, and the Fano factor are given by

$$eI = \frac{G_0}{2} \int_{\mu}^{\mu+eV} d\varepsilon \text{Tr} \left[\hat{\mathcal{T}}(\varepsilon) \right], \quad (10)$$

$$\mathcal{F} = \frac{\mathcal{S}(\omega = 0)}{2eI} = \frac{\int_{\mu}^{\mu+eV} d\varepsilon \text{Tr} \left[\hat{\mathcal{T}}(1 - \hat{\mathcal{T}}) \right]}{\int_{\mu}^{\mu+eV} d\varepsilon \text{Tr} \left[\hat{\mathcal{T}} \right]}. \quad (11)$$

The transmission amplitudes $t_{\alpha\beta}(\varepsilon)$ varies on an energy scale on the order of the level spacing. We focus on the case, when the conditions (7) are satisfied. Then for the \mathcal{F} we have

$$\mathcal{F} = \frac{\text{Tr} \langle \hat{\mathcal{T}}(1 - \hat{\mathcal{T}}) \rangle_{\varepsilon}}{\text{Tr} \langle \hat{\mathcal{T}} \rangle_{\varepsilon}}, \quad (12)$$

where the averaging is taken over a temperature window in the vicinity of the Fermi level in the limit $T \gg \Delta$. In what follows we assume the linearized form of the spectrum, with $\varepsilon = v_F k$, so that the energy averaging is reduced to calculation of the integral $\langle \dots \rangle_{\varepsilon} = \Delta^{-1} \int_0^{\Delta} d\varepsilon (\dots) = \frac{L}{2\pi} \int_0^{2\pi/L} dk (\dots)$.

As seen from (10), the conductance is proportional to the transmission coefficient averaged over the spin and the energy:

$$\mathcal{T} = \text{Tr} \langle \hat{\mathcal{T}} \rangle_{\varepsilon} / 2. \quad (13)$$

Introducing also the average

$$\mathcal{T}_2 = \text{Tr} \langle \hat{\mathcal{T}} \hat{\mathcal{T}} \rangle_{\varepsilon}, \quad (14)$$

one can write the Fano factor in the following form:

$$\mathcal{F} = 1 - \frac{\mathcal{T}_2}{2\mathcal{T}}, \quad (15)$$

In the next two subsections we will discuss calculations that allows one to find \mathcal{F} , using Eq. (15). Technically, the key idea is to present the matrix of transmission amplitudes in a special form, which allows to perform the energy averaging analytically.

B. Conventional AB interferometer

We start with calculation of \mathcal{F} for CI having two arms with the lengths $L/2 \pm a$ and two contacts (not necessarily identical) described by scattering matrices with real amplitudes [see Eq. (2)]. We first find convenient expression for matrix of transmission amplitude (which is a scalar for spinless CI), substitute it into the formula (12), and average over the energy.

1. Method of calculation

We use the method developed in Ref. [13] to sum amplitudes with different winding numbers. We classify all amplitudes of electrons going out of the ring by their direction, either clockwise, (+), or anticlockwise, (-). For CI with identical contacts, the amplitudes describing processes of passing the ring in opposite directions without extra revolutions are given by

$$\begin{pmatrix} \beta_0^+ \\ \beta_0^- \end{pmatrix} = t_{\text{in}} t_{\text{out}} \begin{pmatrix} e^{i(k-2\pi\phi/L)(L/2+a)} \\ e^{i(k+2\pi\phi/L)(L/2-a)} \end{pmatrix}. \quad (16)$$

All other trajectories finishing at the right lead can be obtained recursively, multiplying by a matrix describing processes which increase number of revolutions, clockwise or counterclockwise, by unity (for a more detailed discussion, see Ref. [13]):

$$\begin{pmatrix} \beta_{n+1}^+ \\ \beta_{n+1}^- \end{pmatrix} = \hat{A} \begin{pmatrix} \beta_n^+ \\ \beta_n^- \end{pmatrix},$$

$$\hat{A} = e^{ikL} \begin{pmatrix} t^2 e^{-i2\pi\phi} + t_b^2 e^{i2ka} & tt_b (e^{-i2\pi\phi} + e^{i2ka}) \\ tt_b (e^{i2\pi\phi} + e^{-i2ka}) & t^2 e^{i2\pi\phi} + t_b^2 e^{-i2ka} \end{pmatrix}.$$

The full transmission amplitude across the ring is given by:

$$t^{\text{CI}}(\varepsilon) = \sum_{n=0}^{\infty} \alpha \hat{A}^n \beta_0 = \alpha (1 - \hat{A})^{-1} \beta_0, \quad \alpha = \begin{pmatrix} 1 \\ 1 \end{pmatrix}. \quad (17)$$

Having particular expressions for $t^{\text{CI}}(\varepsilon)$, we get $\mathcal{T}^{\text{CI}}(\varepsilon) = |t^{\text{CI}}(\varepsilon)|^2$ and $\mathcal{T}_2^{\text{CI}}(\varepsilon) = |t^{\text{CI}}(\varepsilon)|^4$. The averaging over ε is reduced to integration over the unit circle in complex plane of $z = e^{ikL}$ and is easily performed by residues, see App A. Most interesting and physically transparent limiting cases are presented below. In the most general case of interferometer with contacts of different strength, the obtained analytical expressions are rather cumbersome and we present them in the Appendix B.

2. Results (symmetric setup, identical contacts)

For the case of a *symmetric* interferometer with equal arm lengths ($a = 0$) and identical contacts, the energy-averaged transmission coefficient [11] is given by

$$\mathcal{T}^{\text{CI}}(\phi, \gamma) = \frac{2\gamma \cos^2(\pi\phi)}{\gamma^2 + \cos^2(\pi\phi)}. \quad (18)$$

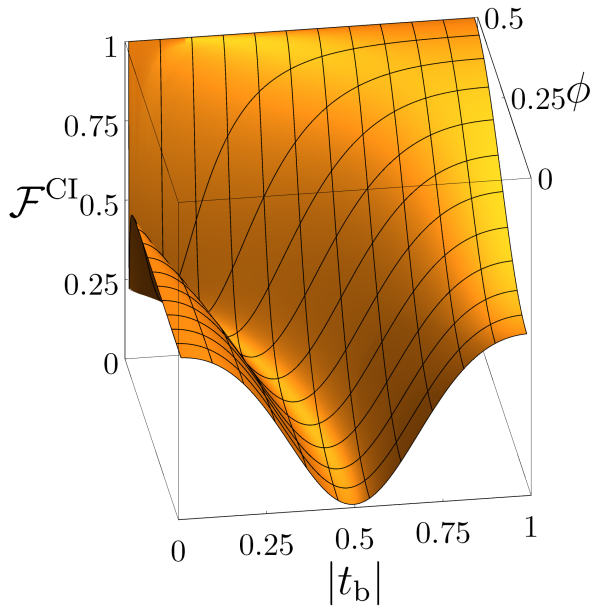


FIG. 5. The dependence of Fano factor, $\mathcal{F}^{\text{CI}}(\phi, t_b)$, on the amplitude of backscattering on the contact, t_b , and the magnetic flux, ϕ , as described by Eqs. (2), (18), (19).

Using formulas from Appendix A we find the Fano factor in the form

$$\mathcal{F}^{\text{CI}}(\phi, \gamma) = 1 - \frac{\cos^2(\pi\phi) [5\gamma^2 + \gamma^4 + (1 + \gamma^2) \cos^2(\pi\phi)]}{2[\gamma^2 + \cos^2(\pi\phi)]^2}. \quad (19)$$

Equation (19) is illustrated in Fig. 5, where the dependence of Fano factor on the magnetic flux and on the backscattering on the contact, $|t_b| = \gamma/(1 + \gamma)$. For three types of tunneling contacts shown in Fig. 3, Eq. (19) simplifies:

$$\begin{aligned} \mathcal{F}^{\text{CI}}(\phi, 0) &= \frac{1}{2}, \\ \mathcal{F}^{\text{CI}}(\phi, \infty) &= 1 - \frac{1}{2} \cos^2(\pi\phi), \\ \mathcal{F}^{\text{CI}}(\phi, 1) &= \frac{4 \sin^2(\pi\phi)}{(\cos(2\pi\phi) + 3)^2}. \end{aligned} \quad (20)$$

The value $1/2$ for $\gamma \rightarrow 0$ is a standard value for the Fano factor of tunneling level. We also note that the “metallic” contacts with $\gamma = 1$, shows both minimal value $\mathcal{F}^{\text{CI}} = 0$, at $\phi = 0$, and to the maximal value, $\mathcal{F}^{\text{CI}} = 1$, at $\phi \rightarrow 1/2$.

The dependencies of \mathcal{T}^{CI} and \mathcal{F}^{CI} on the magnetic flux are shown in Fig. 6a, 6b. The latter figure yielded cross-section of Fig. 5 for fixed γ . We see that the transmission coefficient and the Fano factor have, respectively, sharp antiresonance and sharp resonance at $\phi = 1/2$ (and, consequently, at all half-integer values of the flux).

Several interesting properties of $\mathcal{F}^{\text{CI}}(\phi, \gamma)$ are to be mentioned here. Firstly,

$$\mathcal{F}^{\text{CI}}(0, \gamma) = \mathcal{F}^{\text{CI}}(0, 1/\gamma) = \frac{1}{2} \left(\frac{1 - \gamma^2}{1 + \gamma^2} \right)^2, \quad (21)$$

and also

$$\mathcal{T}^{\text{CI}}(0, \gamma) = \mathcal{T}^{\text{CI}}(0, 1/\gamma) = \frac{2\gamma}{1 + \gamma^2}.$$

It means that for zero flux, the setup with the contacts shown in Fig. 3a with a certain γ is indistinguishable in terms of noise and conductance from the setup with the contacts shown in Fig. 3b with $\gamma_1 = 1/\gamma$.

Let us discuss this point in more detail. As seen from Eqs. (18) and (19), at $\phi = 0$ the Fano factor and the transmission coefficient are related as follows:

$$\mathcal{F}^{\text{CI}} = \frac{1}{2} [1 - (\mathcal{T}^{\text{CI}})^2]. \quad (22)$$

This equation is shown by red curve in Fig. 7 and is valid both for $\gamma < 1$ (i.e. for contacts shown in Fig. 3a) and for $\gamma > 1$ (i.e. for contacts shown in Fig. 3b). Specifically, changing γ from $\gamma = 0$ to $\gamma = \infty$, we pass the red curve twice: once in the interval $0 < \gamma < 1$ and once again for $1 < \gamma < \infty$. This is clearly seen from the cross-section of Fig. at $\phi = 0$. Having in mind to compare below with the HI, we note that the role of the amplitude t_b is somewhat similar to the scattering on the magnetic impurity in case of HI, considered below. For the case of CI, dependence on $|t_b|$ at $\phi = 0$ (i.e. on the red curve Fig. 3a) directly follows from Eq. (21):

$$\mathcal{F}_{\phi=0}^{\text{CI}} = \frac{1}{2} \frac{(|t_b| - 1/2)^2}{2[(|t_b| - 1/2)^2 + 1/4]^2}.$$

Importantly, the Fano factor has minimum with zero minimal value in the “metallic” point, $t_b = 1/2$ ($\gamma = 1$). This property is lost in presence of magnetic flux, see Fig. 5.

For $\phi \neq 0$, the red curve splits into two curves, as shown in Fig. 7 by blue, green and orange lines. Notice that the Fano factor can have two values for the same value of the transmission coefficient, corresponding to two different γ . Remarkably, there is a special singular point, $\phi = 1/2$, where the conductance is exactly zero (see [8] and a more detailed discussion of this property in [11]). At this point, the Fano factor becomes unity for fixed γ :

$$\mathcal{T}^{\text{CI}}(1/2, \gamma) = 0, \quad \mathcal{F}^{\text{CI}}(1/2, \gamma) = 1. \quad (23)$$

The behavior of the Fano factor near this point is illustrated by the orange curve in Fig. 7a, which corresponds to $\phi = 0.48$. The transmission coefficient and the Fano factor for $|\delta\phi| = |\phi - 1/2| \ll 1$, weak tunneling coupling, $\gamma \ll 1$, and arbitrary ratio

$$x = \pi\delta\phi/\gamma.$$

are given by the following expressions

$$\begin{aligned} \mathcal{T}^{\text{CI}}(\delta\phi, \gamma) &\approx 2\gamma \frac{x^2}{1 + x^2}, \\ \mathcal{F}^{\text{CI}}(\delta\phi, \gamma) &\approx \frac{2 - x^2 + x^4}{2(1 + x^2)^2}, \end{aligned} \quad (24)$$

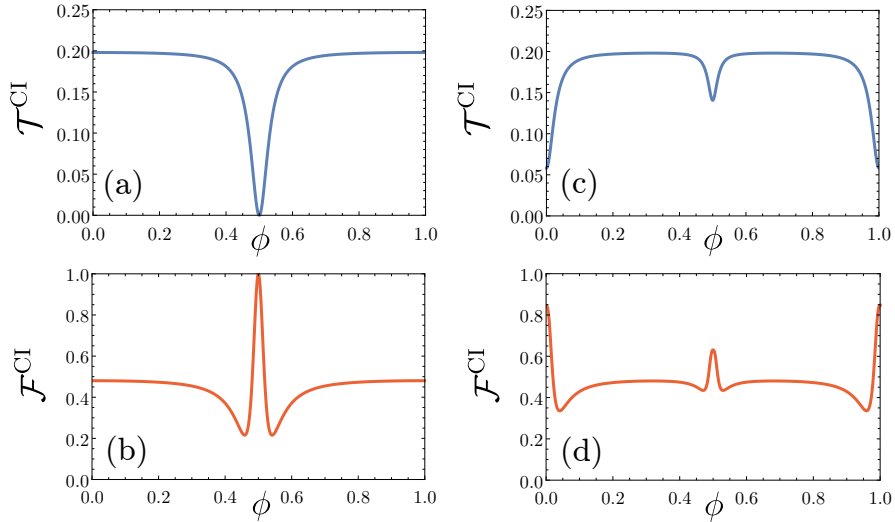


FIG. 6. The transmission coefficient (blue curves) and the Fano factor (red curves) for conventional interferometer with two identical contacts. In *symmetric* interferometer with $a = 0$ and weak tunneling coupling ($\gamma = 0.1$) there is antiresonance in \mathcal{T}^{CI} and resonance in \mathcal{F}^{CI} at half-integer values of the flux [panels (a) and (b)]. In *asymmetric* interferometer with $a \neq 0$ and weak tunneling coupling ($\gamma = 0.1$, $k_F a = 1.0$), there also appear peaks at integer values of the flux [panels (c) and (d)]. With increasing a , peaks at $\phi = 1/2 + n$ decrease in amplitude and become narrower, while peaks at $\phi = n$ grow and become wider (here, n is integer).

Hence, the value of \mathcal{F}^{CI} depends on the order of taking the limits $\delta\phi \rightarrow 0$ and $\gamma \rightarrow 0$, so that if we fix $\delta\phi$ and tend γ to zero, then instead of Eq. (23) we get the usual expression for the tunnel contact:

$$\mathcal{F}^{\text{CI}} \rightarrow 1/2, \quad \gamma \rightarrow 0, \quad \delta\phi \text{ is fixed.}$$

From Eqs. (24) we can get an analytical expression describing the orange line in Fig. 7a. To this end, we fix $\delta\phi$ and change tunneling coupling from $\gamma = 0$ to relatively large value: $\delta\phi \ll \gamma \ll 1$. Then, we get

$$\mathcal{F}^{\text{CI}} \approx \frac{3}{4} - \frac{1}{2} \frac{\mathcal{T}^{\text{CI}}}{\pi\delta\phi} \pm \frac{1}{4} \sqrt{1 - \left(\frac{\mathcal{T}^{\text{CI}}}{\pi\delta\phi}\right)^2}, \quad 0 < \mathcal{T}^{\text{CI}} < \pi|\delta\phi|, \quad (25)$$

The sign in front of the last term distinguish two branches of the orange curve. The minimum of \mathcal{T}^{CI} is reached at the lower branch at $\mathcal{T}^{\text{CI}} = 15\pi|\delta\phi|/16$ and is given by $\mathcal{F}^{\text{CI}} = 17/32$, which is the value of the dashed line in Fig. 7a for $\mathcal{T}^{\text{CI}} = 0$.

In Fig. 7a we fixed ϕ and changed γ from zero to infinity. Fixing γ instead and changing ϕ in the interval $0 < \phi < 1$, we find the following expression connecting transmission coefficient and the Fano factor valid for any γ in the interval $0 < \gamma < \infty$:

$$\mathcal{F}^{\text{CI}} = 1 - \frac{5 + \gamma^2}{2} \frac{\mathcal{T}^{\text{CI}}}{2\gamma} + 2 \left(\frac{\mathcal{T}^{\text{CI}}}{2\gamma}\right)^2, \quad (26)$$

$$0 < \mathcal{T}^{\text{CI}} < \frac{2\gamma}{1 + \gamma^2}.$$

This equation has minimum at $\mathcal{T}_{\text{min}}^{\text{CI}} = (5 + \gamma^2)\gamma/4$ given by $\mathcal{F}_{\text{min}}^{\text{CI}} = [7 - \gamma^2(10 + \gamma^2)]/32$. The family of the curves

described by Eq. (26) for different γ is shown in Fig. 7b. Note that the dashed curves in panels (a) and (b) of Fig. 7 coincide.

3. Results (asymmetric setup)

The asymmetry of setup becomes important when $a \gtrsim k_F^{-1}$. For not too large voltages, $eV \ll v_F/a$, one can replace $ka \rightarrow k_F a$ in scattering amplitudes. The expression for the transmission coefficient in asymmetric setup was obtained earlier in Ref. [11]. Analytical expression for the Fano factor in this case can be found by using formulas presented in Appendixes A and B. Its general form is too cumbersome and we present it here only for the flux values close to integer and half-integer number and for weak tunneling coupling.

For $\delta\phi = |\phi - 1/2| \ll 1$ and $\gamma \ll 1$ the Fano factor reads:

$$\mathcal{F}_{1/2}^{\text{CI}}(\delta\phi, \gamma) = \frac{2 - \bar{x}^2 + \bar{x}^4}{2(1 + \bar{x}^2)^2} + \frac{\sin^2(k_F a)[3\bar{x}^2 - \sin^2(k_F a)]}{2(1 + \bar{x}^2)[\bar{x}^2 + \sin^2(k_F a)]}, \quad (27)$$

where

$$\bar{x} = \frac{\pi\delta\phi}{\gamma \cos(k_F a)}.$$

Similar to Eq. (24), the value of $\mathcal{F}_{1/2}^{\text{CI}}$ at $\delta\phi \rightarrow 0$, $\gamma \rightarrow 0$ depends on the order of limits. Fixing $\delta\phi$ and decreasing the tunneling coupling to zero, $\gamma \rightarrow 0$, we get $\bar{x} \rightarrow \infty$, so that $\mathcal{F}_{1/2}^{\text{CI}} \rightarrow 1/2$. Putting $\delta\phi$ to zero first, we find $\mathcal{F}_{1/2}^{\text{CI}} \rightarrow 1 - (1/2) \sin^2(k_F a)$.

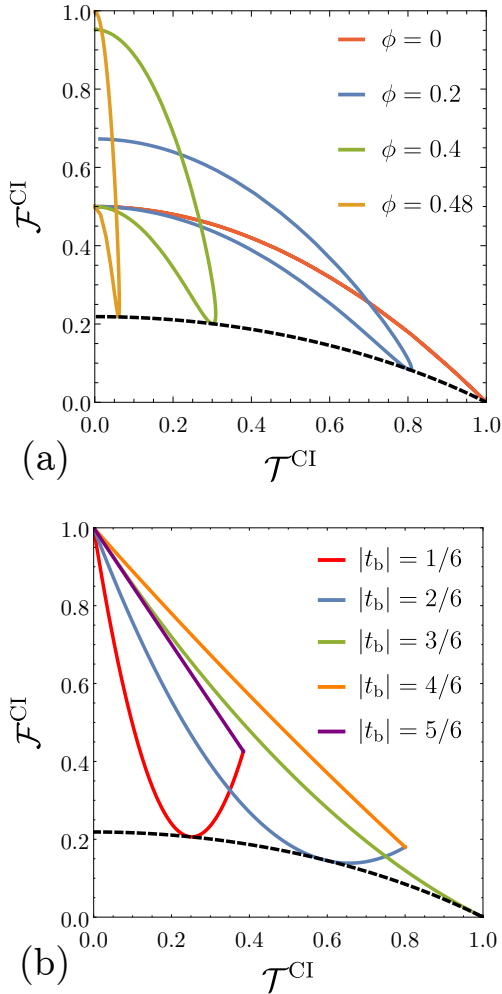


FIG. 7. Parametric plot $(\mathcal{F}^{\text{CI}}, \mathcal{T}^{\text{CI}})$ for fixed ϕ and $0 < \gamma < \infty$ (a), for fixed $|t_b| = \gamma/(1 + \gamma)$ and $0 < \phi < 1$ (b).

It turns out, that the Eq. (27) also describes the case of small magnetic flux, $|\phi| \ll 1$, if we set $\delta\phi = \phi$ there and replace $k_F a$ by $k_F a + \pi/2$.

The dependencies of \mathcal{T}^{CI} and \mathcal{F}^{CI} on the magnetic flux, ϕ , are shown in Fig. 6c and 6d. Comparing these figures with Fig. 6a and 6b plotted for symmetric case, we see that new peaks at integer values of the flux appear for $a \neq 0$ both in the transmission coefficient and in the Fano factor.

4. Results (different tunneling couplings)

In this subsection, we present results for the case of symmetric setup, $a = 0$, but different right and left contacts, characterized by parameter, γ_R and γ_L , respectively. Using general equations presented in Appendix B and performing standard energy averaging with the use of formulas from Appendix A, one can find the following expressions for the transmission coefficient and Fano

factor:

$$\begin{aligned} \mathcal{T}^{\text{CI}}(\phi, \gamma_R, \gamma_L) &= \kappa^{-1/2} \frac{2\bar{\gamma} \cos^2(\pi\phi)}{\bar{\gamma}^2 + \cos^2(\pi\phi)}, \\ \mathcal{F}^{\text{CI}}(\phi, \gamma_R, \gamma_L) &= 1 - \kappa^{-1} \frac{\cos^2(\pi\phi)}{2(\bar{\gamma}^2 + \cos^2(\pi\phi))^2} \\ &\times ((1 + 4\kappa)\bar{\gamma}^2 + \bar{\gamma}^4 + (1 + \bar{\gamma}^2) \cos^2(\pi\phi)), \end{aligned} \quad (28)$$

where

$$\bar{\gamma} = \sqrt{\gamma_L \gamma_R}, \quad \kappa = (\gamma_L + \gamma_R)^2 / 4\gamma_L \gamma_R.$$

The analog of Eq. (22) at $\phi = 0$ for different right and left contacts attains the form

$$\mathcal{F}^{\text{CI}} = 1 - \frac{1}{2\kappa} - \frac{\kappa}{2} (\mathcal{T}^{\text{CI}})^2. \quad (29)$$

C. Helical AB interferometer

Next, we discuss the Fano factor of the current noise in HI having two arms with lengths L_1 and L_2 . Just as in the case of CI we start formula for energy dependent amplitude $t^{\text{HI}}(\varepsilon)$, which is a matrix in spinful case, and then perform energy averaging. The analytical expression obtained for \mathcal{F}^{HI} is rather cumbersome, so we present it in the Appendix C focusing in the main text on the most interesting limiting cases.

1. Scattering matrix

The matrix of the transmission amplitudes t^{HI} from one contact to another is defined as follows

$$\begin{pmatrix} a^\uparrow \\ a^\downarrow \end{pmatrix} = t^{\text{HI}} \begin{pmatrix} b^\uparrow \\ b^\downarrow \end{pmatrix}, \quad (30)$$

where $(b^\uparrow, b^\downarrow)$ and $(a^\uparrow, a^\downarrow)$ are the amplitudes of incoming (from the left contact) and outgoing (to the right contact) waves, respectively (see Fig. 1). This matrix has been obtained earlier [17]:

$$\begin{aligned} \hat{t}^{\text{CI}} &= \frac{r^2 e^{2\pi i \phi L_1 / L}}{t^2} \begin{pmatrix} e^{ikL_1} & 0 \\ 0 & e^{-ikL_1} \end{pmatrix} \begin{pmatrix} t & 0 \\ 0 & 1 \end{pmatrix} \hat{g} \begin{pmatrix} t & 0 \\ 0 & 1 \end{pmatrix}, \\ \hat{g} &= \cos \theta \left[\begin{pmatrix} 0 & 0 \\ 0 & -1 \end{pmatrix} + \frac{1}{2} \sum_{\alpha=\pm 1} \frac{1 + \alpha \hat{H}}{1 - t^2 e^{i(kL + \alpha 2\pi\phi_0)}} \right]. \end{aligned} \quad (31)$$

Here, t and r are scattering amplitudes entering matrix Eq. (3), ϕ_0 is determined by the relation

$$\cos(2\pi\phi_0) = \cos \theta \cos(2\pi\phi), \quad (32)$$

and the matrix \hat{H} is given by

$$\hat{H} = \begin{pmatrix} a & be^{i\xi} \\ be^{-i\xi} & -a \end{pmatrix}, \quad (33)$$

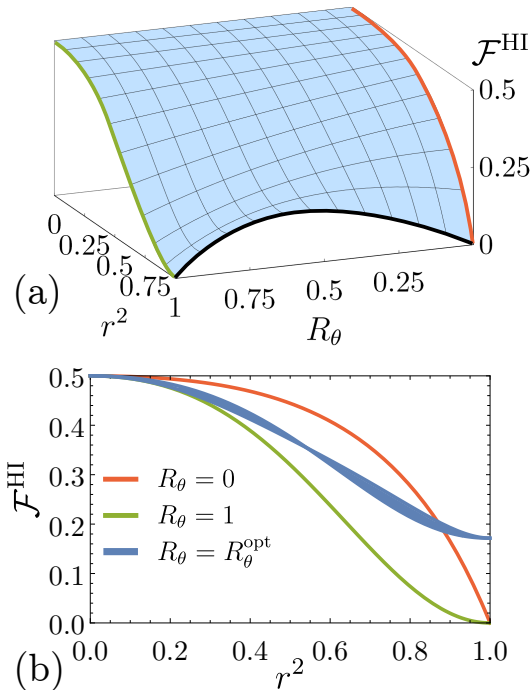


FIG. 8. Panel (a): The dependence of the Fano factor, \mathcal{F}^{HI} , on r^2 and the strength of the magnetic impurity, R_θ ; for $r \rightarrow 1$ there is an optimal value, $R_\theta = R_\theta^{\text{opt}}$, where the Fano factor has maximum. Panel (b): Cross-sections of panel (a) at different values of R_θ ; dependence on the flux is weak and is illustrated for $R_\theta = R_\theta^{\text{opt}}$ by broadening of the curve (shown by blue color) for flux belonging to interval $0 < \phi < 1$.

where ξ is defined in Eq. (6). The coefficients

$$a = i \frac{e^{-2\pi i \phi} - \cos(2\pi \phi_0) \cos \theta}{\cos \theta \sin(2\pi \phi_0)}, \quad (34)$$

$$b = \frac{e^{-2\pi i \phi} \tan \theta}{\sin(2\pi \phi_0)}, \quad (35)$$

are related by the relation $a^2 + b^2 = 1$.

Calculations shows that asymmetry of the arms does not play any role in the HI. Also, position of MD x_0 drops out from final expressions for \mathcal{T}^{HI} and \mathcal{F}^{HI} . We therefore consider two cases: identical contacts (see next subsection and Appendix C 1) and non-identical contacts (see Appendix C 2)

Generalization of Eq. (31) for the case of different tunneling contacts characterized by amplitudes t_L and t_R is straightforward. One should make in this equation the following replacement:

$$t \rightarrow \sqrt{t_L t_R}, \quad r \rightarrow \sqrt{r_L r_R}, \quad \xi \rightarrow \xi + i\beta,$$

where the parameter describing the difference of tunneling contacts [see also App. C 2] is

$$\beta = \frac{1}{2} \ln(t_R/t_L). \quad (36)$$

2. Results (identical contacts)

The transmission coefficient and the Fano factor are obtained with the use of Eqs. (9), (13), (14), (15), and (31). Direct energy averaging in Eqs. (13) and (14) yields

$$\mathcal{T}^{\text{HI}} = \tanh \lambda \left[1 - \frac{\sin^2 \theta \sinh^2 \lambda \cosh(2\lambda)}{\cosh^2(2\lambda) - \cos^2 \theta \cos^2(2\pi \phi)} \right] \quad (37)$$

and

$$\mathcal{T}_2^{\text{HI}} = \tilde{C} \sum_{m,n=0}^3 \tilde{A}_{(m,n)} \frac{\sinh^{2n} \lambda}{D^m}. \quad (38)$$

Here

$$\begin{aligned} D &= \sinh^2(2\lambda) + R_\theta + (1 - R_\theta)R_\phi, \\ \tilde{C} &= \tanh \lambda / \cosh^2 \lambda, \\ R_\theta &= \sin^2 \theta, \quad R_\phi = \sin^2(2\pi \phi), \end{aligned} \quad (39)$$

and the coefficients $\tilde{A}_{(m,n)}$ depend on R_θ , R_ϕ do not depend on λ . Analytical expressions for these coefficients are presented in the Appendix C. The Fano factor is connected with \mathcal{T}^{HI} and $\mathcal{T}_2^{\text{HI}}$ by Eq. (15).

In Fig. 8a, we present dependence of the Fano factor, on r^2 and the strength of the magnetic impurity, R_θ for $\phi = 0$. For “metallic” contact, $r \rightarrow 1$, dependence of the backscattering strength R_θ is non-monotonous. Comparing this figure with analogous Fig. 20 for CI, we see that in both cases the Fano factor has extremum as a function of squared backscattering amplitude. However, for CI the Fano factor has minimum, while for HI it has maximum.

In Fig. 8b, we plot dependence of \mathcal{F}^{HI} on r^2 for fixed R_θ . Two limiting dependencies, corresponding to absence of impurity, $R_\theta = 0$, and very strong impurity, $R_\theta = 1$, are shown by orange and green line, respectively. In both cases, there is no dependence on the magnetic flux. For any other R_θ in the interval $0 < R_\theta < 1$, the Fano factor depends on ϕ but this dependence is much weaker as compared to CI. Each curve corresponding to certain R_θ broadens as illustrated by blue curve corresponding to $R_\theta = R_\theta^{\text{opt}}$.

In order to emphasize this dependence one can consider normalized value

$$\mathcal{F}_n^{\text{HI}}(\phi) = \frac{\mathcal{F}^{\text{HI}}(\phi) - \mathcal{F}^{\text{HI}}(1/4)}{\mathcal{F}^{\text{HI}}(0) - \mathcal{F}^{\text{HI}}(1/4)}. \quad (40)$$

The dependence of the normalized quantity $\mathcal{F}_n^{\text{HI}}$ on the magnetic flux for several sets of parameters R_θ and λ is shown in Fig. 9 along with the flux dependence of the normalized transmission coefficient. One can see sharp resonances both in $\mathcal{F}_n^{\text{HI}}$ and $\mathcal{T}_n^{\text{HI}}$ at weak tunneling coupling and small R_θ (see Fig. 9c) which evolve into harmonic Aharonov-Bohm oscillations with increasing λ and R_θ (see Fig. 9d)

One can also plot dependence of the Fano factor on the transmission coefficient similar to Fig. 7 for CI. Analogous dependence for HI is shown in Fig. 10. Interesting

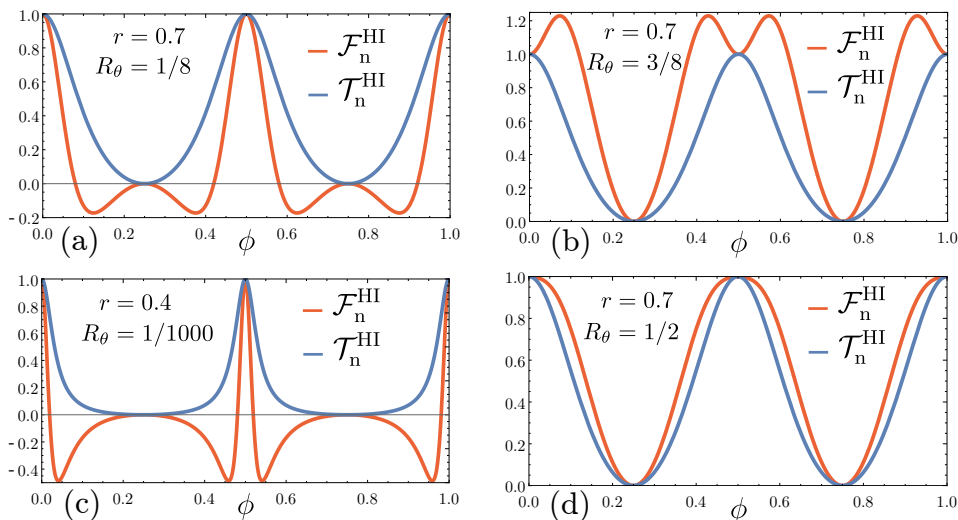


FIG. 9. Dependence of the normalized factor Fano, $\mathcal{F}_n^{\text{HI}}$, and the normalized conductance, $\mathcal{T}_n^{\text{HI}}$, for the helical interferometer on magnetic flux, ϕ , at different strengths of scattering by a magnetic defect R_θ and tunneling amplitude, r . (a) $r = 0.7, R_\theta = 1/8$ (b) $r = 0.7, R_\theta = 3/8$ (c) $r = 0.4, R_\theta = 1/1000$ (d) $r = 0.7, R_\theta = 1/2$.

difference of two pictures is that CI has a single noiseless point, $\mathcal{F}^{\text{CI}} = 0$, corresponding to ideal transmission, $\mathcal{T}^{\text{CI}} = 1$, while HI in addition to the analogous point with $\mathcal{F}^{\text{HI}} = 0$, $\mathcal{T}^{\text{HI}} = 1$ has one more noiseless point, corresponding to $R_\theta = 1$, $\lambda = \infty$. At this point $\mathcal{F}^{\text{HI}} = 0$, $\mathcal{T}^{\text{HI}} = 1/2$.

3. Limiting cases

Here, we discuss several limiting cases allowing for simple analytical description.

In the absence of a magnetic defect, $R_\theta = 0$, interference effects are absent as we discussed in the introduction, so that expressions for the Fano factor and transmission coefficient dramatically simplify:

$$\mathcal{T}^{\text{HI}} = \tanh[\lambda], \quad \mathcal{F}^{\text{HI}} = \frac{1}{2 \cosh^2[\lambda]}. \quad (41)$$

These equations not depend on ϕ and are related by the same equation as for ballistic CI [compare with Eq. (22)]

$$\mathcal{F}^{\text{HI}} = \frac{1}{2} [1 - (\mathcal{T}^{\text{HI}})^2]. \quad (42)$$

This dependence is shown in Fig. 10 by red line

The formulas for the conductance and Fano factor in case of different tunneling contacts can also be obtained in closed form and are presented in Appendix C2. An analog of Eq. (42) in case of different tunneling contacts, in contrast to CI case, cf. Eq. (29) looks a bit more cumbersome

$$\mathcal{F}^{\text{HI}} = \frac{[1 - (\mathcal{T}^{\text{HI}})^2] \sqrt{\sinh^2(2\beta) + (\mathcal{T}^{\text{HI}})^2}}{\sqrt{\sinh^2(2\beta) + (\mathcal{T}^{\text{HI}})^2 + \mathcal{T}^{\text{HI}} \cosh(2\beta)}}, \quad (43)$$

with the asymmetry parameter $\beta = \frac{1}{2} \ln(t_R/t_L)$, Eq. (36).

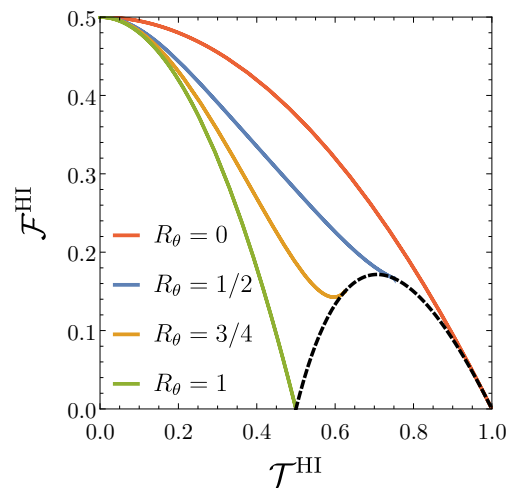


FIG. 10. The combined dependence of Fano factor, \mathcal{F}^{HI} , and the transmission coefficient, \mathcal{T}^{HI} , on the transparency of the contact, λ , for different strength of the magnetic impurity, R_θ , and the magnetic flux $\phi = 0.4$, according to Eqs. (37), (38). The black dashed line borders the area of maximum transmission coefficient for given R_θ .

The Fano factor and transmission coefficient also do not depend on the magnetic flux for the strong magnetic impurity, $R_\theta = 1$ (green curves on the Fig. 8, accordingly). In this case, we have

$$\mathcal{T}^{\text{HI}} = \frac{1}{2} \tanh[2\lambda], \quad \mathcal{F}^{\text{HI}} = \frac{1}{2 \cosh^2[2\lambda]}, \quad (44)$$

$$\mathcal{F}^{\text{HI}} = \frac{1}{2} - 2 (\mathcal{T}^{\text{HI}})^2.$$

Last dependence is shown by green line in Fig. 10.

The flux dependence is also absent for the open interferometer, $r = 1$ ($\lambda = \infty$). In this case, we get

$$\begin{aligned}\mathcal{T}^{\text{HI}} &= 1 - \frac{R_\theta}{2}, \\ \mathcal{F}^{\text{HI}} &= R_\theta \frac{1 - R_\theta}{2 - R_\theta} = \frac{(2\mathcal{T}^{\text{HI}} - 1)(1 - \mathcal{T}^{\text{HI}})}{\mathcal{T}^{\text{HI}}}.\end{aligned}\quad (45)$$

Hence, the Fano factor has a maximum as a function of backscattering probability as is shown by the black curve in the Fig. 8 (b).

Equation (45) has a simple physical meaning. For $r = 1$, the windings are absent, and there are two parallel conductors, i.e. lower and upper arms of the HI. The lower arm, with spin \downarrow , is an ideal conductor with the transmission coefficient $\mathcal{T}_\downarrow = 1$ while the transmission through the upper arm is controlled by the magnetic defect, $\mathcal{T}_\uparrow = \cos^2 \theta$, varying from 0 to 1. Then, we get

$$\mathcal{F}^{\text{HI}} = \frac{\mathcal{T}_\uparrow(1 - \mathcal{T}_\uparrow)}{1 + \mathcal{T}_\uparrow}.\quad (46)$$

Taking into account that the total transmission coefficient in this case is given by $\mathcal{T}^{\text{HI}} = (\mathcal{T}_\uparrow + 1)/2$, we arrive to Eq. (45). We have maximum $\mathcal{F}_{\text{max}}^{\text{HI}} = 3 - 2\sqrt{2} \approx 0.17$ at $\mathcal{T}_{\uparrow, \text{max}} = \sqrt{2} - 1$ and, respectively, $R_\theta^{\text{max}} = 2 - \sqrt{2} \approx 0.59$. The total transmission coefficient at this point is given by $\mathcal{T}_{\text{max}}^{\text{HI}} = 1/\sqrt{2}$. We notice that Eq. (45) describes both green line in Fig. 10 and dashed black line in Fig. 10.

For almost metallic contact, $t \ll 1$ ($\lambda \rightarrow \infty$), and for an arbitrary scattering strength on a magnetic defect, \mathcal{F}^{HI} shows weak oscillations with ϕ :

$$\begin{aligned}\mathcal{F}^{\text{HI}} &\approx \frac{R_\theta(1 - R_\theta)}{2 - R_\theta} + 2t^2 \\ &+ 2t^4 \frac{R_\theta(1 - R_\theta)(10 - 12R_\theta + 3R_\theta^2)}{(2 - R_\theta)^2} \cos(4\pi\phi).\end{aligned}\quad (47)$$

More interesting is the opposite case of an almost tunnel contact: $t \rightarrow 1$, $r = \sqrt{1 - t^2} \ll \theta$. In this case,

$$\mathcal{F}^{\text{HI}} \approx \frac{1}{2} - \frac{r^4}{8} \left[1 + \frac{3R_\theta}{R_\phi + R_\theta - R_\theta R_\phi} \right].\quad (48)$$

This formula shows weak but sharp resonances with magnetic flux. These resonances are well pronounced in the normalized Fano factor. Indeed, from Eq. (48) for $\theta \ll 1$ we obtain

$$\mathcal{F}_n^{\text{HI}} \approx \frac{\theta^2}{\theta^2 + \sin^2(2\pi\phi)},$$

i.e. sharp resonances at $\phi = 0$ and $\phi = 1/2$.

IV. DISCUSSION AND CONCLUSION

In the previous sections we analyzed two types of quantum interferometers based on conventional materials and

helical edge states. We have demonstrated that Fano factor in both systems is substantially modified by quantum interference effects. It is essential that the interference effects survive in the high temperature limit, $T \gg \Delta$. The appearance of temperature-robust interference effects stems from trajectories interfering at any energy. In case of symmetric CI for any trajectory entering the interferometer and moving clockwise there is another trajectory moving counterclockwise, and these trajectories interfere destructively at $\phi = 1/2$. Such destructive interference is exact, i.e. the transmission amplitude is identically zero at all energies, $t(\epsilon, \phi = 1/2) \equiv 0$ [8] (see also the discussion of the consequences of this identity in [11, 14]). As a result, conventional interferometers demonstrate anti-resonances in conductance, $\mathcal{T}^{\text{CI}} \rightarrow 0$, and resonances in Fano factor, $\mathcal{F}^{\text{CI}} \rightarrow 1$, at half-integer flux values [see Eqs. (14) and (15)]. For asymmetric CI there also appear peaks of different height and width at integer flux values. Both \mathcal{T}^{CI} and \mathcal{F}^{CI} are periodic in flux with a period $\Delta\phi = 1$.

The peculiarity of interference effects in helical interferometer lies in the fact that they appear only in presence of backscattering defects. In this case trajectories interfering at any energy appear as well, namely, trajectories returning to the defect after n revolutions clockwise and counterclockwise are always interfering. The relative phase of such trajectories is $4\pi n\phi$, and as a result the Aharonov-Bohm oscillation period in HI equals to $\Delta\phi = 1/2$. Thus we have a similarity between the ballistic CI where the scattering at the contacts is always present and HI with backward scatterers.

Interestingly, at $\phi = 0$, the dependence of the \mathcal{F}^{CI} on the transmission coefficient is given by the same formula for the ballistic helical and the conventional interferometers [see Eqs. (22) and (42)]. However, this equation fails for conventional interferometer for $\phi \neq 0$ so that two branches in the dependence $\mathcal{F}^{\text{CI}}(\mathcal{T}^{\text{CI}})$ arise due to the fact that the same conductance can be realized in a conventional interferometer by contacts of different types [see panels (a) and (b) of the Fig. 3].

To conclude, we have developed a theory of shot noise in quantum Aharonov-Bohm interferometers under condition $T \gg \Delta$, Eq. (1), and described in detail two cases: (i) conventional single-channel spinless interferometer and (ii) interferometer based on helical edge states. We demonstrated that in both cases the interference effects strongly modify the shot noise. We have derived general analytical expressions for the Fano factor and demonstrated a resonant behavior of \mathcal{F} on ϕ both for CI and HI in the regime of weak tunneling coupling to the leads. The resonant peaks are located at integer and half-integer values of the magnetic flux. An exception is the case of CI with the interferometer arms of equal length, when \mathcal{F} exhibits only resonances at half-integer values of the flux, $\phi = 1/2 + n$ with integer n , similarly to anti-resonances in conductance. The resonant peaks are found to be much more pronounced for CI. In HI even in the regime of well pronounced resonances the relative change

in \mathcal{F} in the whole range of ϕ is quite small ($\lesssim 0.1$), with resonances having small amplitude and appearing on the top of high background value of \mathcal{F} . In both CI and HI, the amplitude of peaks decreases when decreasing the tunneling coupling. For completely closed CI and HI rings, peaks disappear while $\mathcal{F} \rightarrow 1/2$. For metallic contacts, \mathcal{F} does not depend on ϕ for HI and shows weakly non-linear oscillations with ϕ for CI. The magnetic defect strongly *enhances* the \mathcal{F}^{HI} , and there is an optimal value of the defect strength $\theta_{\text{max}} \approx 0.28\pi$, providing the maximum value of the Fano factor, $\mathcal{F}_{\text{max}}^{\text{HI}} \approx 0.17$. On the contrary, for the weak tunneling contacts, the magnetic defect *reduces* \mathcal{F}^{HI} . In the ballistic CI, \mathcal{F}^{CI} also depends on backscattering, defined by the contacts. Similar to HI, there is an optimal value of backscattering, however, in contrast to HI, \mathcal{F}^{CI} has a minimum at this point.

Before closing the paper we make several comments regarding possible experimental measurements of the Fano factor. As for conventional interferometer, it shows different noise for the same transmission coefficient (see, for example, Fig. 7). Hence, measuring, complementary to conductance, also the Fano factor would allow one to determine the type of the tunneling coupling (see Fig. 3a and Fig. 3b) and its strength. In the helical interfer-

ometer, measurement of both conductance and the Fano factor would allow one to find probability of backscattering that violate topological protection. Indeed, as seen from Fig. 10 values of \mathcal{T}^{HI} and \mathcal{F}^{HI} unambiguously determines the value of the backscattering probability R_θ . Also, measurement of the flux dependence of the normalized Fano factor and transmission coefficient would allow one to determine type of the contacts. For tunneling contacts and sufficiently weak backscattering we predict sharp resonant behavior of both quantities on the flux (see Fig. 9c), while for the case of “metallic” contact and strong backscattering both Fano factor and conductance would show harmonic Aharonov-Bohm oscillations (see Fig. 9d).

ACKNOWLEDGMENTS

The work was carried out with financial support from the Russian Science Foundation (grant No. 20-12-00147-II). The work of R.A. Niyazov was also partially supported by the Theoretical Physics and Mathematics Advancement Foundation “BASIS”.

Appendix A: Energy averaging

Throughout the paper we average observable quantities over a small temperature window in the vicinity of the Fermi level in the limit $T \gg \Delta$. For the linearized form of the spectrum, with $\varepsilon = v_F k$, the energy averaging is reduced at high temperatures to calculating the integral $\langle \dots \rangle_\varepsilon = \Delta^{-1} \int_0^\Delta d\varepsilon (\dots) = \frac{L}{2\pi} \int_0^{2\pi/L} dk (\dots)$. The averaging over kL , is reduced to integration over the unit circle $z = e^{ikL}$ in complex plane and is easily performed by residues. The formulas which were used for calculations are listed below:

$$\begin{aligned}
 \left\langle \prod_{j=1}^4 \frac{1}{(1 - \tau_j e^{\alpha i k L})^{n_j}} \right\rangle_\varepsilon &= 1, \quad n_j = 0, 1, \\
 \left\langle \frac{1}{(1 - \tau_1 e^{\alpha i k L})} \frac{1}{(1 - \tau_2 e^{-\alpha i k L})} \right\rangle_\varepsilon &= \frac{1}{1 - \tau_1 \tau_2}, \\
 \left\langle \frac{1}{(1 - \tau_1 e^{\alpha i k L})} \frac{1}{(1 - \tau_2 e^{-\alpha i k L})} \frac{1}{(1 - \tau_3 e^{-\alpha i k L})} \right\rangle_\varepsilon &= \frac{1}{(1 - \tau_1 \tau_2)(1 - \tau_1 \tau_3)}, \\
 \left\langle \frac{1}{(1 - \tau_1 e^{\alpha i k L})} \frac{1}{(1 - \tau_2 e^{-\alpha i k L})} \frac{1}{(1 - \tau_3 e^{-\alpha i k L})} \frac{1}{(1 - \tau_4 e^{-\alpha i k L})} \right\rangle_\varepsilon &= \frac{1}{(1 - \tau_1 \tau_2)(1 - \tau_1 \tau_3)(1 - \tau_1 \tau_4)}, \\
 \left\langle \frac{1}{(1 - \tau_1 e^{\alpha i k L})} \frac{1}{(1 - \tau_2 e^{\alpha i k L})} \frac{1}{(1 - \tau_3 e^{-\alpha i k L})} \frac{1}{(1 - \tau_4 e^{-\alpha i k L})} \right\rangle_\varepsilon &= \frac{1 - \tau_1 \tau_2 \tau_3 \tau_4}{(1 - \tau_1 \tau_3)(1 - \tau_2 \tau_3)(1 - \tau_1 \tau_4)(1 - \tau_2 \tau_4)},
 \end{aligned} \tag{A1}$$

where $\alpha = \pm 1$ and all $|\tau_j| < 1$.

Appendix B: Conventional interferometer with non-equal arms and non-identical contacts

In this Appendix, we present generalization of the tunneling amplitude $t^{\text{CI}}(\varepsilon)$ [see Eq. (17)] for the case of non-identical contacts having different tunneling couplings. The symmetric case is obtained by putting $t_{\text{in,L}} = t_{\text{in,R}} = t_{\text{in}}$,

etc. in equations presented below.

$$t^{\text{CI}}(\varepsilon) = \sum_{n=0}^{\infty} \vec{\alpha} \hat{A}^n \vec{\beta}_0, \quad \vec{\alpha} = \begin{pmatrix} 1 \\ 1 \end{pmatrix}, \quad \vec{\beta} = \begin{pmatrix} \beta_0^+ \\ \beta_0^- \end{pmatrix} = t_{\text{in,L}} t_{\text{out,R}} \begin{pmatrix} e^{i(k-2\pi\phi/L)(L/2+a)} \\ e^{i(k+2\pi\phi/L)(L/2-a)} \end{pmatrix}, \quad (\text{B1})$$

$$\hat{A} = e^{ikL} \begin{pmatrix} t_{\text{L}} t_{\text{R}} e^{-i2\pi\phi} + t_{\text{b,L}} t_{\text{b,R}} e^{i2ka} & t_{\text{L}} t_{\text{b,R}} e^{-i2\pi\phi} + t_{\text{b,L}} t_{\text{R}} e^{i2ka} \\ t_{\text{L}} t_{\text{b,R}} e^{i2\pi\phi} + t_{\text{b,L}} t_{\text{R}} e^{-i2ka} & t_{\text{L}} t_{\text{R}} e^{i2\pi\phi} + t_{\text{b,L}} t_{\text{b,R}} e^{-i2ka} \end{pmatrix}.$$

After some algebra one can rewrite expression for $t^{\text{CI}}(\varepsilon)$ as follows:

$$t(\varepsilon)^{\text{CI}} = t_{\text{in,L}} t_{\text{out,R}} e^{-i2\pi\phi a/L} \left(\frac{Z e^{i(kL/2-\pi\phi)}}{1 - \tilde{t}^2 e^{ikL-2\pi\phi}} + \frac{Z^* |_{\text{L} \leftrightarrow \text{R}} e^{i(kL/2+\pi\phi)}}{1 - \tilde{t}^{*2} e^{ikL+2\pi\phi}} \right),$$

$$Z = i \frac{Z_1 Z_2}{Z_3} e^{i\pi\phi},$$

$$Z_1 = Z_4 - (t_{\text{b,L}} - t_{\text{L}})(t_{\text{b,R}} \sin(2ak) + t_{\text{R}} \sin(2\pi\phi)) - i(t_{\text{b,R}} t_{\text{L}} \cos(2ak) + t_{\text{b,L}} t_{\text{R}} \cos(2\pi\phi)),$$

$$Z_2 = Z_4 + (t_{\text{b,R}} - t_{\text{R}})(t_{\text{b,L}} \sin(2ak) + t_{\text{L}} \sin(2\pi\phi)) - i(t_{\text{b,L}} t_{\text{R}} \cos(2ak) + t_{\text{b,R}} t_{\text{L}} \cos(2\pi\phi)),$$

$$Z_3 = 2Z_4 \left(t_{\text{b,L}} t_{\text{R}} e^{-i(ak+\pi\phi)} + t_{\text{b,R}} t_{\text{L}} e^{i(ak+\pi\phi)} \right),$$

$$Z_4^2 = (t_{\text{b,L}}^2 - t_{\text{L}}^2) (t_{\text{b,R}}^2 - t_{\text{R}}^2) - (t_{\text{b,L}} t_{\text{b,R}} \cos(2ak) + t_{\text{L}} t_{\text{R}} \cos(2\pi\phi))^2,$$

$$\tilde{t}^2 = iZ_4 + t_{\text{b,L}} t_{\text{b,R}} \cos(2ak) + t_{\text{L}} t_{\text{R}} \cos(2\pi\phi).$$
(B2)

Assuming that $eV \ll v_F/a$, one can replace $ka \rightarrow k_F a$ in this equation. Now we see that the expressions $|t^{\text{CI}}(\varepsilon)|^2$, $|t^{\text{CI}}(\varepsilon)|^4$ contain the complex quantity e^{ikL} which is regarded as a new variable. Then, one can perform averaging of these expressions over energy by using formulad derived in Appendix A.

Appendix C: Helical case

1. Identical contacts

General formulas for the conductance and the noise intensity are obtained by averaging the expressions (8), (9), (10) and (11) in the main text over the energy, using expressions for the amplitude (31). It is convenient to write the resulting formulas, using the parameters λ , R_θ and R_ϕ instead of the parameters t , θ and ϕ , according to the following definitions:

$$t = e^{-\lambda}, \quad r = \sqrt{1 - e^{-2\lambda}}, \quad 0 < \lambda < \infty, \quad (\text{C1})$$

$$R_\theta = \sin^2 \theta, \quad (\text{C2})$$

$$R_\phi = \sin^2(2\pi\phi). \quad (\text{C3})$$

Direct calculation of energy averages in formulas (13) and (14) yields

$$\mathcal{T}^{\text{HI}} = C \sum_{m,n=0}^1 A_{(m,n)} \frac{\sinh^{2n} \lambda}{D^m}, \quad (\text{C4})$$

$$\mathcal{T}_2^{\text{HI}} = \tilde{C} \sum_{m,n=0}^3 \tilde{A}_{(m,n)} \frac{\sinh^{2n} \lambda}{D^m}, \quad (\text{C5})$$

with

$$D = \sinh^2(2\lambda) + R_\theta + (1 - R_\theta)R_\phi,$$

$$C = \tanh \lambda,$$

$$A_{(0,0)} = 1 - R_\theta/2,$$

$$A_{(0,1)} = 0,$$

$$A_{(1,0)} = R_\theta(R_\theta + (1 - R_\theta)R_\phi)/2,$$

$$A_{(1,1)} = R_\theta,$$
(C6)

which leads to Eq. (37) and

$$\begin{aligned}
\tilde{C} &= \tanh \lambda / \cosh^2 \lambda, \\
\tilde{A}_{(0,0)} &= 1 + R_\theta(1 - R_\theta/2), \\
\tilde{A}_{(0,1)} &= 2 - R_\theta(2 - R_\theta), \\
\tilde{A}_{(1,0)} &= R_\theta^2(R_\theta + R_\phi(1 - R_\theta))/4, \\
\tilde{A}_{(1,1)} &= R_\theta(R_\theta - 4(1 - R_\theta)(3 - 2R_\theta)(1 - R_\phi))/2, \\
\tilde{A}_{(2,0)} &= -R_\theta(2 - R_\theta)(R_\theta + R_\phi(1 - R_\theta))^2/2, \\
\tilde{A}_{(2,1)} &= -R_\theta(R_\theta(1 - R_\phi) + R_\phi) \\
&\quad \times (R_\theta(13 - 9R_\theta(1 - R_\phi) - 17R_\phi) + 8R_\phi)/2, \\
\tilde{A}_{(2,2)} &= -R_\theta(R_\theta(9 - 7R_\theta(1 - R_\phi) - 11R_\phi) + 4R_\phi), \\
\tilde{A}_{(3,0)} &= -R_\theta^2(R_\theta + R_\phi(1 - R_\theta))^3/4, \\
\tilde{A}_{(3,1)} &= -3R_\theta^2(R_\theta + R_\phi(1 - R_\theta))^3/2, \\
\tilde{A}_{(3,2)} &= -3R_\theta^2(R_\theta + R_\phi(1 - R_\theta))^2, \\
\tilde{A}_{(3,3)} &= -R_\theta^2(4 - 2R_\theta(1 - R_\phi) - 2R_\phi) \\
&\quad \times (R_\theta(1 - R_\phi) + R_\phi), \\
\tilde{A}_{(0,2)} = \tilde{A}_{(0,3)} = \tilde{A}_{(1,2)} = \tilde{A}_{(1,3)} = \tilde{A}_{(2,3)} &= 0.
\end{aligned} \tag{C7}$$

2. Non-identical contacts

In general case the tunneling rates in different contacts of the interferometer are described by unequal tunneling amplitudes

$$\begin{aligned}
t_{R,L} &= te^{\pm\beta}, \quad |\beta| \leq \lambda \\
t_R t_L &= e^{-2\lambda}, \\
t_R/t_L &= e^{2\beta}.
\end{aligned} \tag{C8}$$

In this case we may still use the expressions (C4), (38), but the coefficients should be redefined, $A_{(m,n)} \rightarrow A_{(m,n)}^u$, $\tilde{A}_{(m,n)} \rightarrow \tilde{A}_{(m,n)}^u$, as follows

$$\begin{aligned}
C^u &= C \left(1 - \frac{\sinh^2 \beta}{\sinh^2 \lambda} \right), \\
A_{(0,0)}^u &= A_{(0,0)}, \\
A_{(0,1)}^u &= 0, \\
A_{(1,0)}^u &= A_{(1,0)} + R_\theta \sinh^2 \beta, \\
A_{(1,1)}^u &= A_{(1,1)} + 2R_\theta \sinh^2 \beta, \\
\tilde{C}^u &= \tilde{C} \left(1 - \frac{\sinh^2 \beta}{\sinh^2 \lambda} \right)^2, \\
\tilde{A}_{(0,0)}^u &= \tilde{A}_{(0,0)} + 2R_\theta(2 - R_\theta) \sinh^2 \beta, \\
\tilde{A}_{(0,1)}^u &= \tilde{A}_{(0,1)}, \\
\tilde{A}_{(1,0)}^u &= \tilde{A}_{(1,0)} + R_\theta(12 - R_\theta(17 - 9R_\theta)) \\
&\quad - 3(1 - R_\theta)(4 - 3R_\theta)R_\phi + 4R_\theta \sinh^2 \beta \sinh^2 \beta/2, \\
\tilde{A}_{(1,1)}^u &= \tilde{A}_{(1,1)} + R_\theta^2 \sinh^2(2\beta), \\
\tilde{A}_{(2,0)}^u &= \tilde{A}_{(2,0)} + R_\theta(R_\theta(1 - R_\phi) + R_\phi) \\
&\quad \times (R_\theta(13 - 7R_\theta(1 - R_\phi) - 11R_\phi) \\
&\quad - 4(2 - R_\phi)) \sinh^2 \beta/2 \\
&\quad + 5R_\theta^2(1 - R_\theta)(1 - R_\phi) \sinh^4 \beta, \\
\tilde{A}_{(2,1)}^u &= \tilde{A}_{(2,1)} - 4R_\theta(2 - R_\theta)(R_\theta(1 - R_\phi) + R_\phi) \sinh^2 \beta \\
&\quad + 10R_\theta^2(1 - R_\theta)(1 - R_\phi) \sinh^4 \beta, \\
\tilde{A}_{(2,2)}^u &= \tilde{A}_{(2,2)} - 2R_\theta(R_\theta(9 - 7R_\theta(1 - R_\phi) - 11R_\phi) \\
&\quad + 4R_\phi) \sinh^2 \beta, \\
\tilde{A}_{(3,0)}^u &= \tilde{A}_{(3,0)} - R_\theta^2(R_\theta(1 - R_\phi) + R_\phi) \\
&\quad \times ((R_\theta(1 - R_\phi) + R_\phi)(2 - R_\theta(1 - R_\phi) - R_\phi) \\
&\quad + (4 - 3R_\theta(1 - R_\phi) - 3R_\phi) \sinh^2 \beta) \sinh^2 \beta, \\
\tilde{A}_{(3,1)}^u &= \tilde{A}_{(3,1)} - 6R_\theta^2(R_\theta(1 - R_\phi) + R_\phi)(R_\theta(1 - R_\phi) + R_\phi) \\
&\quad + (2 - R_\theta(1 - R_\phi) - R_\phi) \sinh^2 \beta) \sinh^2 \beta, \\
\tilde{A}_{(3,2)}^u &= \tilde{A}_{(3,2)} - 12R_\theta^2(R_\theta(1 - R_\phi) + R_\phi)(R_\theta(1 - R_\phi) \\
&\quad + R_\phi + \sinh^2 \beta) \sinh^2 \beta, \\
\tilde{A}_{(3,3)}^u &= \tilde{A}_{(3,3)} - 2R_\theta^2(R_\theta(1 - R_\phi) + R_\phi) \sinh^2(2\beta), \\
\tilde{A}_{(0,2)}^u &= \tilde{A}_{(0,3)}^u = \tilde{A}_{(1,2)}^u = \tilde{A}_{(1,3)}^u = \tilde{A}_{(2,3)}^u = 0.
\end{aligned} \tag{C9}$$

-
- [1] Y. Aharonov and D. Bohm, Phys. Rev. **115**, 485 (1959).
[2] Y. Aharonov and D. Bohm, Phys. Rev. **130**, 1625 (1963).
[3] B. Bernevig and T. Hughes, *Topological Insulators and Topological Superconductors* (Princeton University Press, 2013).
[4] M. Z. Hasan and C. L. Kane, Rev. Mod. Phys. **82**, 3045 (2010).
[5] X.-L. Qi and S.-C. Zhang, Rev. Mod. Phys. **83**, 1057 (2011).
[6] M. J. M. de Jong and C. W. J. Beenakker, in *Mesoscopic Electron Transport*, NATO ASI Series E, Vol. 345, edited by L. Sohn, L. Kouwenhoven, and G. Schön (Kluwer Academic Publishing, Dordrecht, 1997) pp. 225–258.
[7] Y. Blanter and M. Büttiker, Phys. Rep. **336**, 1 (2000).
[8] M. Büttiker, Y. Imry, and M. Y. Azbel, Phys. Rev. A **30**, 1982 (1984).
[9] M. Büttiker, Y. Imry, R. Landauer, and S. Pinhas, Phys. Rev. B **31**, 6207 (1985).
[10] E. A. Jagla and C. A. Balseiro, Phys. Rev. Lett. **70**, 639 (1993).
[11] A. P. Dmitriev, I. V. Gornyi, V. Y. Kachorovskii, and D. G. Polyakov, Phys. Rev. Lett. **105**, 036402 (2010).

- [12] P. M. Shmakov, A. P. Dmitriev, and V. Y. Kachorovskii, *Phys. Rev. B* **85**, 75422 (2012).
- [13] P. M. Shmakov, A. P. Dmitriev, and V. Y. Kachorovskii, *Phys. Rev. B* **87**, 235417 (2013).
- [14] A. P. Dmitriev, I. V. Gornyi, V. Y. Kachorovskii, D. G. Polyakov, and P. M. Shmakov, *JETP Lett.* **100**, 839 (2015).
- [15] A. P. Dmitriev, I. V. Gornyi, V. Y. Kachorovskii, and D. G. Polyakov, *Phys. Rev. B* **96**, 115417 (2017).
- [16] R. A. Niyazov, D. N. Aristov, and V. Y. Kachorovskii, *Phys. Rev. B* **98**, 045418 (2018).
- [17] R. A. Niyazov, D. N. Aristov, and V. Y. Kachorovskii, *npj Comput. Mater.* **6** (2020), 10.1038/s41524-020-00442-z.
- [18] R. A. Niyazov, D. N. Aristov, and V. Y. Kachorovskii, *Phys. Rev. B* **103**, 125428 (2021).
- [19] R. A. Niyazov, D. N. Aristov, and V. Y. Kachorovskii, *JETP Lett.* **113**, 689 (2021).
- [20] R. A. Niyazov, D. N. Aristov, and V. Y. Kachorovskii, *Phys. Rev. B* **108**, 075424 (2023).
- [21] K. Kobayashi and M. Hashisaka, *J. Phys. Soc. Jpn.* **90**, 102001 (2021).
- [22] J. M. Edge, J. Li, P. Delplace, and M. Büttiker, *Phys. Rev. Lett.* **110**, 246601 (2013).
- [23] F. Dolcini, *Phys. Rev. B* **92**, 155421 (2015).
- [24] S. Munyan, A. Rashidi, A. C. Lygo, R. Kealhofer, and S. Stemmer, *Nano Lett.* **23**, 5648 (2023).
- [25] N. Lezmy, Y. Oreg, and M. Berkooz, *Phys. Rev. B* **85**, 235304 (2012).
- [26] A. Del Maestro, T. Hyart, and B. Rosenow, *Phys. Rev. B* **87**, 165440 (2013).
- [27] E. S. Tikhonov, D. V. Shovkun, V. S. Khrapai, Z. D. Kvon, N. N. Mikhailov, and S. A. Dvoretzky, *JETP Lett.* **101**, 708 (2015).
- [28] K. E. Nagaev, S. V. Remizov, and D. S. Shapiro, *JETP Lett.* **108**, 664 (2018).
- [29] J. I. Väyrynen and L. I. Glazman, *Phys. Rev. Lett.* **118**, 106802 (2017).
- [30] S. U. Piatrusha, L. V. Ginzburg, E. S. Tikhonov, D. V. Shovkun, G. Koblmüller, A. V. Bubis, A. K. Grebenko, A. G. Nasibulin, and V. S. Khrapai, *JETP Lett.* **108**, 71 (2018).
- [31] P. D. Kurilovich, V. D. Kurilovich, I. S. Burmistrov, Y. Gefen, and M. Goldstein, *Phys. Rev. Lett.* **123**, 056803 (2019).
- [32] V. D. Kurilovich, P. D. Kurilovich, I. S. Burmistrov, and M. Goldstein, *Phys. Rev. B* **99**, 085407 (2019).
- [33] B. V. Pashinsky, M. Goldstein, and I. S. Burmistrov, *Phys. Rev. B* **102**, 125309 (2020).
- [34] C.-H. Hsu, P. Stano, J. Klinovaja, and D. Loss, *Semicond. Sci. Tech.* **36**, 123003 (2021).
- [35] B. Probst, P. Virtanen, and P. Recher, *Phys. Rev. B* **106**, 085406 (2022).
- [36] P. P. Aseev and K. E. Nagaev, *Phys. Rev. B* **94**, 045425 (2016).
- [37] E. Olshanetsky, G. Gusev, A. Levin, Z. Kvon, and N. Mikhailov, *Phys. Rev. Lett.* **131**, 076301 (2023).
- [38] D. N. Aristov and P. Wölfle, *Phys. Rev. B* **84**, 155426 (2011).
- [39] D. N. Aristov, A. P. Dmitriev, I. V. Gornyi, V. Y. Kachorovskii, D. G. Polyakov, and P. Wölfle, *Phys. Rev. Lett.* **105**, 266404 (2010).
- [40] D. N. Aristov, I. V. Gornyi, D. G. Polyakov, and P. Wölfle, *Phys. Rev. B* **95**, 155447 (2017).
- [41] D. V. Khomitsky, A. A. Konakov, and E. A. Lavrukina, *J. Phys. Condens. Matter* **34**, 405302 (2022).
- [42] V. A. Sablikov and A. A. Sukhanov, *Phys. Rev. B* **103**, 155424 (2021).